Dynamic Characterization of an Adaptive Film-Riding Seal

Joshua Bird[1], Patrick Keogh[1], Carl Sangan[1],
Aaron Bowsher[2], Peter Crudington[2], and James Scobie[1]
jb3315@bath.ac.uk, p.s.keogh@bath.ac.uk, c.m.sangan@bath.ac.uk,
aaron.bowsher@crossmanufacturing.com,
pete.crudgington@crossmanufacturing.com, and j.a.scobie@bath.ac.uk
[1]Department of Mechanical Engineering
University of Bath
Bath, BA2 7AY
United Kingdom
[2]Cross Manufacturing Co. (1938) Ltd.
Devizes
United Kingdom

ABSTRACT

Shaft seals control the leakage of fluid between areas of high pressure and low pressure around rotating components inside turbomachinery. Static seals are often subject to damaging rubs with the shaft, caused by assembly misalignments and rotordynamic vibrations during operation. Adaptive seals aim to reduce leakage flows whilst minimizing wear. The Film Riding Pressure Actuated Leaf Seal (FRPALS) is one such design which utilizes a large installation clearance and is blown down towards the shaft under pressure.

This paper presents a numerical model which can be used in the design and development of adaptive shaft seals, validated by experimental data from the literature. The model uses a modified version of the Reynolds equation to predict the dynamic, frequency-dependent stiffness and damping coefficients of the fluid film. The dynamic coefficients have been solved for different operational clearances and pressure differences to generate coefficient maps. These maps have been incorporated into a blow down model with compliant mechanical leaves to predict the transient

translational and angular displacement paths of the FRPALS when subject to an increasing pressure drop.

The blow down model has been compared against experimental measurements collected from a specially designed test facility for the characterization of shaft seal performance. Eddy current probes were used to measure the displacement paths of the FRPALS with the experimental values showing that the model can accurately predict the dynamic movement of the seal when subject to a pressure difference.

1 INTRODUCTION

Sealing in turbomachinery is one of the most cost-effective methods of enhancing engine efficiency and performance [1], critical to reaching net-zero power generation and propulsion. Shaft seals play a crucial role in the Secondary Air System (SAS), used to cool critical parts in the turbine, seal bearing chambers and balance forces on high-pressure components. Figure 1 shows a cross-section of a typical high bypass aircraft engine with several key sealing locations in the SAS network highlighted. These seals are used to control the clearance and control leakage flows between rotating and static components.

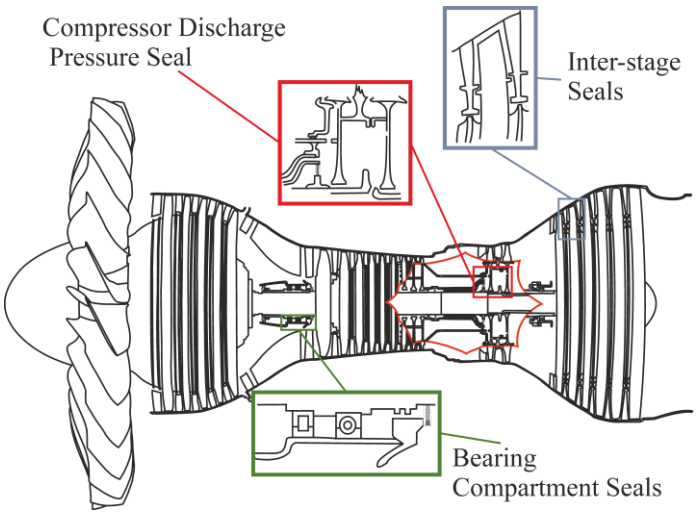

Figure 1: Cross-section of a high by-pass engine with a cut-away showing a simplified SAS and several key sealing locations.

Labyrinth seals are typical in gas turbines; they are simple in design, of relatively low cost to manufacture and allow shaft rotation in either direction. However, labyrinth seals suffer from rubs that increase leakage and often lead to aero-elastic instabilities. Compliant designs such as brush seals can be manufactured to minimize the clearance with the rotor, achieving reduced leakage and increased rub tolerance. They can accommodate excursions of the rotor due to start-up and shut-down operations and other transient procedures but can be damaged under large eccentric motion, resulting in wear and reduced operational life.

To address the performance limitations of traditional turbomachinery seals, a new generation of adaptive sealing technology is currently under development. One such example is the Film Riding Pressure Actuated Leaf Seal (FRPALS), a non- contacting compliant seal that can adapt to varying clearances without rubbing, while maintaining low leakage. This seal features a large installation clearance to allow for eccentric shaft motion under low pressure, and will blow down towards the rotor at operating

conditions, decreasing the clearance to minimize leakages. This process is demonstrated in Fig. 2 (a), where the seal design is shown to comprise of a hydrodynamic runner connected to a seal housing via a series of compliant leaves. The upstream leaves are used for positioning and allow for the outer surface of the runner to be subjected to high-pressure flow. The downstream sealing leaves reduce the leakage flow passing through the seal. The runner features a Rayleigh Step on the inner surface to generate a pressure gradient so that the seal film rides. The resulting fluid film in between the shaft and runner prevents the seal from contact with the rotor. To fully seal around the circumference of the shaft, the FRPALS is made up of segments which can actuate independently of one another. They are held together in the casing as shown in Fig 2 (b).

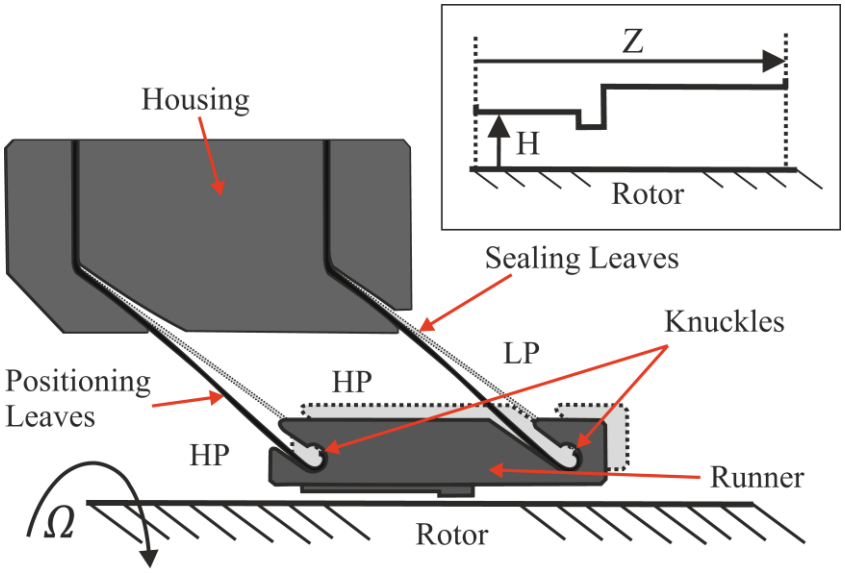

(a)

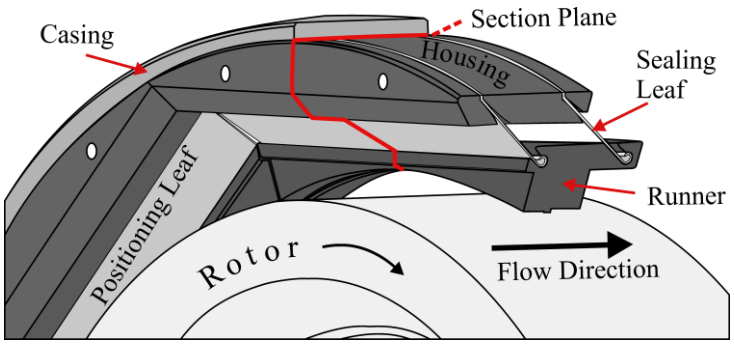

(b)

Figure 2: (a) FRPALS blow down when pressurized and the Rayleigh step geometry in detail view. (b) 3D view of segment in-situ showing the section plane of 2D projection in the center of the runner.

The force from the working fluid can be conveniently modeled as a spring-damper system with a stiffness, K, and damping, C, a method developed by Black [1] and Childs [2]. This concept may be further expanded to a 360° fluid film with both direct and cross-coupled dynamic coefficients. A positive direct stiffness (K) and direct damping (C) are stabilizing. However, a positive cross-coupled stiffness (k) would excite the

rotor and should be minimized for a dynamically stable system [3]. The magnitude of force from the working fluid depends on the seal clearance. This means that the clearance affects the stability of the system and so must be considered throughout the design process [4].

This paper presents a numerical approach for predicting the dynamic coefficients and blow down behavior of an adaptive seal. The Reynolds equation [5] is used to predict the pressure distribution in the thin fluid film. Results from the numerical model were then compared with experimental measurements of the FRPALS from a dynamic high-speed rig for two runner geometries.

Section 2 discusses different sealing technologies and theoretical techniques used to model their behavior. Section 3 presents a numerical model for predicting dynamic coefficients, which are then used in Section 4 to determine the compliant seal dynamic behavior. The model incorporates the Reynolds equation to predict the dynamic film pressures, together with experimentally determined mechanical leaf characteristics. The predictions of the dynamic coefficients and blow down are compared with experimental results and shown to be accurate for two FRPALS geometries.

2 LITERATURE REVIEW

Labyrinth seals are a common sealing solution in turbomachinery that can withstand very large pressure drops of over 300 bar [6]. The leakage flow is restricted through a series of cascading cavities, which maximizes internal frictional forces and turbulence, thereby dissipating the kinetic energy of the working fluid [7]. The acceleration and deceleration of the working fluid through the cascading cavities is, however, inherently

unsteady. In some cases, this motion can lead to rotor excitation and turbomachine instability [8].

As described by Ferguson [9], the brush seal offered the first viable alternative to the labyrinth seal for turbomachinery applications. The compliant nature of the brush seal improves system stability by reducing the unsteady eccentricities associated with a labyrinth seal [10]. However, they are subject to wear under all conditions, as the bristle pack rests on the rotor, and are also prone to aerodynamic flutter.

The Hydrostatic Advanced Low Leakage (HALO) seal is based on the use of shoes in the seal design for reducing leakage flow and wear. The HALO seal uses radially soft, axially stiff sealing cantilever beams to support the sealing shoes. The shoes are designed to choke the gas flow as the runner actuates toward the rotor. A reaction force prevents the seal and rotor from making contact, hence, it may be classified as a film riding seal [11]. The HALO seal was used to replace the existing labyrinth seals in a hydrogen compressor, which was shown to operate more efficiently at full speed [12]. San Andrés and Anderson [11] tested a HALO seal up to 6 bar at temperatures up to 300°C and showed that the seal exhibited 50% less leakage flow than an equivalent labyrinth seal.

To overcome the rotordynamic instabilities of labyrinth seals and the comparatively short operational life of brush seals, the leaf seal was developed [13]. The leaf seal comprises of a series of thin metal plates, known as ‘leaves’, layered around the circumference of the shaft. The leaves are designed to rest on the shaft and lift off and film ride when subject to hydrodynamic forces [14].

Grondahl [15] developed the Pressure Actuated Leaf Seal (PALS) where the leaves are aligned with the rotor and actuate when subject to pressure, which prevents leakage

flow through the gaps between the leaves. Grondahl [16] showed that the PALS had less than 50% of the leakage flow of an equivalent four-toothed labyrinth seal. Furthermore, Bowsher *et al.* [17] tested a prototype PALS seal up to 8.3 bar with the shaft rotating up to 20,000 rpm. The rub on the leaves caused an increase in temperature and burrs to form on the tips, however, there was no major loss in performance. Pasch and Stapp [18] successfully implemented PALS into a supercritical carbon dioxide turbocompressor with pressure drops of 130 bar.

The PALS concept was further developed into the FRPALS with the addition of a hydrodynamic shoe or runner to generate a pressure gradient to ensure the seal film rides. Kirk *et al.* [19] conducted preliminary static tests on a large-scale 2D concept design, where the seal was pressurized up to 3.5 bar without shaft rotation. The runner was shown to reduce to approximately 4% of the original clearance as the upstream pressure increased. Additionally, the leaves exhibited little hysteresis during depressurization. The runner exhibited rock, where the seal closed unevenly towards the rotor, however, this was smaller than 0.07 degrees. Pedraza-Valle [20] developed the test facility used in this study for the characterization of seals, including the FRPALS. He found that the position of the Rayleigh Step affected the closure of the seal and the leakage underneath the runner.

2.1 Modeling Adaptive Seals and Thin Fluid Films

Beermann *et al.* [21] developed a 2D CFD model to predict the radial movement of a HALO seal which was compared with experimental results. The study showed that the seal actuated towards the rotor when subject to an upstream pressure, and the CFD

model was able to accurately replicate this behavior. However, the model did not consider circumferential forces.

In the development of the FRPALS, Grondahl and Dudley [22] conducted a series of initial calculations based on preliminary design parameters. Their analysis assumed that the stiffness of the leaves was dependent on the modulus of elasticity and the leaf thickness. The force from the fluid film was assumed to be dependent on a linear pressure drop between the inlet and outlet of the runner. The fluid film analysis identified a seal runner geometry with an adequate hydrostatic radial lifting force to maintain a non-contacting seal clearance at normal operating conditions and over a large range of rotor eccentricity with respect to the seal.

Du *et al*. [23] modeled the leakage under the padded members of a non-contacting finger seal. The semi-analytical model used the Reynolds equation to analyze the seal leakage performance as a function of the seal clearance. The model considered the static stiffness of the fluid film due to a rotor excursion and found the force in the fluid through the difference in pressure profiles generated. This approach was used iteratively to find how the static stiffness of the film varied with rotor displacement.

Faira and San Andrés [24] describe three different numerical methods for calculating the pressure distribution in a high-speed hydrodynamic gas bearing using the Reynolds equation. The numerical model was then used to find the load capacity in slider and Rayleigh step bearings, which was shown to give accurate and stable solutions for high-speed incompressible flows. Gabriel [25] and Faria [26] used the Reynolds equation to model leakage flow and pressure distribution in spiral groove gas face seals. The method was shown to be computationally efficient and accurate at high rotational speeds [26]. The Reynolds equation was used to predict the dynamic stiffness

and damping coefficients for a Rayleigh step bearing by Zhu and San Andrés [27]. They reported that for synchronous speeds the estimated stiffness coefficients offered good agreement with the experimental values. However, the damping coefficients were between two and five times smaller than the predicted values.

This paper presents a numerical model that uses the Reynolds equation to accurately predict the frequency-dependent dynamic coefficients for Rayleigh step components in various displacements and orientations. The dynamic coefficients are then used in an adaptive model to predict the blow down performance of a film-riding seal.

3 FLUID FILM MODELING

This section presents a numerical dynamic model for fluid film seals with experimental validation. This is used in Section 4 to characterize the blow down of a single runner of the FRPALS. A one-dimensional disk growth model, which increases with $\Omega^2\, r^2$ has been used to reduce the clearance with a given rotational speed [28].

3.1 Pressure Profile Modeling

The non-dimensional form of the Reynolds equation in a cylindrical coordinate system is

$$\frac{\partial}{\partial Z}\left(H^3\frac{\partial P^2}{\partial Z}\right)+\frac{\partial}{\partial \theta}\left(H^3\frac{\partial P^2}{\partial \theta}\right)=\Lambda\frac{\partial (PH)}{\partial \theta}+\sigma\frac{\partial (PH)}{\partial t} \tag{1}$$

where θ is the circumferential coordinate and $Z = z/r$ is the axial coordinate. $P = p/p_{atm}$ and $H = h/s$ are the non-dimensionless pressure and film thickness terms,

respectively. Λ is the Compressibility or Bearing Number, and σ the Squeeze Number, which are defined by

$$\Lambda = \frac{6\,\mu\,\Omega\,r^2}{p_{atm}\,s^2} \qquad\qquad \sigma = \frac{12\,\mu\,\omega\;r^2}{p_{atm}\,s^2} \tag{2}$$

The Bearing Number considers changes in pressure profile due to the rotational speeds of the system. The Squeeze Number considers unsteady changes in the pressure profile due to any excitation of the fluid.

Castelli and Pirvics [29] developed a method for solving the Reynolds equation using the dependent variable $Q = P^2H^2$. Eq. (1) can be re-written in terms of Q:

$$\mathfrak{L}(H,Q)Q = \beta(H,Q)\frac{\partial Q}{\partial t} \tag{3}$$

where $\mathfrak{L}(H,Q)$ is the partial differential operator

$$\mathfrak{L}(H,Q) = \frac{\partial^2}{\partial Z^2} + \frac{\partial^2}{\partial \theta^2} - \frac{1}{H}\left(\frac{\partial H}{\partial \theta} + \frac{\Lambda}{\sqrt{Q}}\right)\frac{\partial}{\partial \theta} - \frac{1}{H}\frac{\partial H}{\partial Z}\frac{\partial}{\partial Z} - \frac{2}{H}\left(\frac{\partial^2 H}{\partial Z^2} + \frac{\partial^2 H}{\partial \theta^2}\right) \tag{4}$$

and

$$\beta(H,Q) = \frac{\sigma}{H\sqrt{Q}} \tag{5}$$

3.2 Fluid Film Stiffness and Damping Coefficients

In the event of eccentric movement of the rotor or seal, the film thickness will vary with time-dependent perturbations in orthogonal directions, x and y. Assuming the perturbations are harmonic and small in amplitude the variation of film thickness in complex form is

$$H = H_0 + Xe^{i\omega t}\cos\theta + Ye^{i\omega t}\sin\theta \tag{6}$$

where X and Y are the non-dimensional perturbation amplitudes. The dynamic components of the pressure profile and the dependent variable can be expressed by the first-order Taylor series expansions

$$P = P_0 + P_{ex}Xe^{i\omega t} + P_{ey}Ye^{i\omega t} + O\left(\frac{X^2}{{H_0}^2}, \frac{Y^2}{{H_0}^2}\right) \tag{7}$$

$$Q = Q_0 + Q_{ex}Xe^{i\omega t} + Q_{ey}Ye^{i\omega t} + O\left(\frac{X^2}{{H_0}^2}, \frac{Y^2}{{H_0}^2}\right) \tag{8}$$

P_{ex} and P_{ey} are dimensionless complex dynamic coefficients of pressure in the x and y directions, respectively. Similarly, Q_{ex} and Q_{ey} are the dimensionless complex dynamic coefficients of the dependent variable. The real parts of Q_{ex} and Q_{ey} may be associated with the stiffness characteristics of the fluid, and the imaginary part with the damping characteristics in the respective axes. Eq. 8 can be substituted into Eqs. (3) – (5) which leads to the following equations:

$$\mathfrak{Q}(H_0, Q_0)Q_0 = 0 \tag{9}$$

$$\mathfrak{Q}(H_0, Q_0)Q_{ex} + [\alpha(H_0, Q_0) - \beta(H_0, Q_0)i\omega]Q_{ex} = R_x(H_0, Q_0) \tag{10}$$

$$\mathfrak{Q}(H_0, Q_0)Q_{ey} + [\alpha(H_0, Q_0) - \beta(H_0, Q_0)i\omega]Q_{ey} = R_y(H_0, Q_0) \tag{11}$$

where

$$\alpha(H_0, Q_0) = \frac{1}{2}\left(\frac{\Lambda}{H_0\sqrt{Q_0}}\frac{\partial \ln(Q_0)}{\partial\theta}\right) \tag{12}$$

and

$$\begin{aligned} R_x = & -\frac{\partial Q_0}{\partial\theta}\left(\frac{1}{H_0}\frac{\partial H_0}{\partial\theta}\frac{\cos\theta}{H_0} + \frac{\sin\theta}{H_0} + \frac{1}{H_0}\frac{\Lambda}{\sqrt{Q_0}}\frac{\cos\theta}{H_0}\right) \\ & -\left(\frac{1}{H_0}\frac{\partial H_0}{\partial Z}\frac{\cos\theta}{H_0}\frac{\partial Q_0}{\partial Z}\right) \\ & -\left(\frac{2Q_0}{H_0}\cos\theta\right)\left(1 + \frac{1}{H_0}\left(\frac{\partial^2 H_0}{\partial Z^2} + \frac{\partial^2 H_0}{\partial\theta^2}\right)\right) \end{aligned} \tag{13}$$

and

$$\begin{aligned} R_y = & -\frac{\partial Q_0}{\partial\theta}\left(\frac{1}{H_0}\frac{\partial H_0}{\partial\theta}\frac{\sin\theta}{H_0} + \frac{\cos\theta}{H_0} + \frac{1}{H_0}\frac{\Lambda}{\sqrt{Q_0}}\frac{\sin\theta}{H_0}\right) \\ & -\left(\frac{1}{H_0}\frac{\partial H_0}{\partial Z}\frac{\sin\theta}{H_0}\frac{\partial Q_0}{\partial Z}\right) \\ & -\left(\frac{2Q_0}{H_0}\sin\theta\right)\left(1 + \frac{1}{H_0}\left(\frac{\partial^2 H_0}{\partial Z^2} + \frac{\partial^2 H_0}{\partial\theta^2}\right)\right) \end{aligned} \tag{14}$$

Eq. (9) is the steady-state version of Eq. (3), while Eqs. (10) and (11) define the perturbation coefficients in Eq. (8), which are driven by the first-order coefficients R_x and R_y. The direct pressure perturbation coefficients in Eq. (7) may then be determined through

$$P_{\begin{Bmatrix} ex \\ ey \end{Bmatrix}} = \frac{Q_{\begin{Bmatrix} ex \\ ey \end{Bmatrix}}}{2P_0 \, {H_0}^2} - \frac{P_0 \begin{Bmatrix} \cos\theta \\ \sin\theta \end{Bmatrix}}{H_0} \tag{15}$$

which can be used to calculate the stiffness and damping coefficients of the fluid film, using an integration method defined by Lund and Thomsen [30]. The real parts of Eq (14) may be used to calculate the dimensionless stiffness damping coefficients from

$$\begin{bmatrix} \overline{K}_{xx} \\ \overline{K}_{xy} \end{bmatrix} = -\int_0^L \int_0^{\theta_c} Re(P_{ex}) \begin{bmatrix} \cos\theta \\ \sin\theta \end{bmatrix} d\theta \, dZ \tag{16}$$

and the imaginary parts of Eq (14) can be used to find the dimensionless damping coefficients:

$$\begin{bmatrix} \bar{C}_{xx} \\ \bar{C}_{xy} \end{bmatrix} = -\int_0^L \int_0^{\theta_c} Im(P_{ex}) \begin{bmatrix} \cos\theta \\ \sin\theta \end{bmatrix} d\theta \, dZ \tag{17}$$

The dimensional coefficients may be obtained from

$$K_{ab} = \frac{2rp_{atm}}{c} \overline{K}_{ab} \qquad\qquad C_{ab} = \frac{rp_{atm}}{\omega\pi c} \bar{C}_{ab} \tag{18}$$

Due to the $i\omega$ term in Eqs. (10) and (11), the dynamic coefficients are frequency-dependent.

3.3 Solution Methods and Preliminary Validation

Castelli and Pirvics [29] developed a method for solving the steady-state solution, Q_0. The method divides the film region into a rectangular mesh which is discretized in

the axial (j) and tangential (n) directions. Eq. (4) is discretized using a three-point central difference approximation of the derivatives of Q_0, and the coefficients of each derivative are assembled in a matrix notation:

$$[\Gamma_j]\{Q_j\} + [\Delta_j]\{Q_{j-1}\} + [\Xi_j]\{Q_{j+1}\} = \{R_j\} \tag{19}$$

where $[\Gamma_j]$, $[\Delta_j]$, and $[\Xi_j]$, are $N \times N$ matrices of coefficients respectively, and $\{R_j\}$ is the right-hand side vector defined by Castelli and Pirvics [29]. An iterative process is required to solve for Q_0. Initial estimates at the film inlet, $Q_0 = {P_{in}}^2 H_0^2$, and at the film outlet, $Q_0 = {P_{out}}^2 H_0^2$, may be linearly interpolated along axial film boundaries. The matrices in Eq (18) may be modified for Eqs. (10) and (11) by incorporating Eqs. (12) – (14) to enable numerical solutions for Q_{ex} and Q_{ey}.

The dynamic model developed in this section was used to predict the stiffness and damping coefficients for a Rayleigh step bearing tested by Zhu and San Andrés [27]. The experimental bearing was designed with a clearance of 40 μm, and tested at 2.4 bar pressure drop up to rotational speeds of 5,230 rad/s. The numerical predictions are in good agreement with the experimental values for synchronous frequencies, as evident in Figs. 3 and 4 with experimental results from Zhu and San Andrés [27].

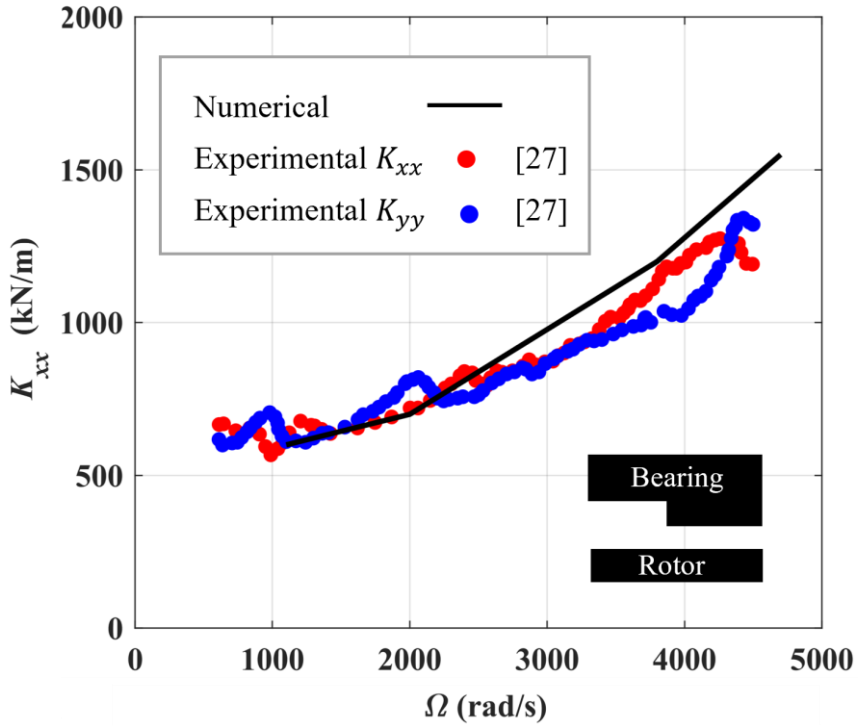

Figure 3: Stiffness coefficient numerical results with experimental data from Zhu and San Andrés [27].

Figure 3 shows that the numerical model and experimental data demonstrate an increase in stiffness coefficient with increasing rotational speed. The numerical model predicts the damping coefficient with the correct order of magnitude and provides approximately the average of the experimental results in the two directions as shown in Fig. 4.

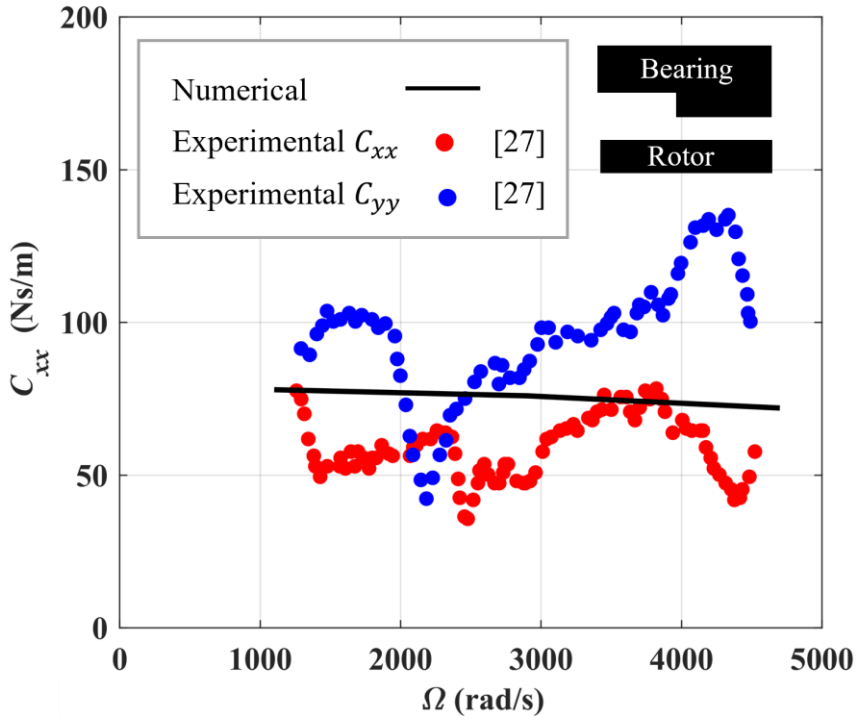

Figure 4: Damping coefficient numerical results with experimental data from Zhu and San Andrés [27].

3.4 Characterization of a Fixed Rayleigh Step Seal

To validate further the numerical model, experimental results documented by Pedraza-Valle [20] are utilized. A cross-section of the test facility is shown in Fig. 5, from which dynamic coefficients and leakage characteristics of an annular Rayleigh step seal with a clearance of 165 μm were measured. The step was designed to the same specifications as the runner geometry detailed by Pedraza-Valle *et al*. [31]. A summary of the lengths and heights are shown in Table 1.

Table 1: Rayleigh Step Geometry for the FRPALS

Parameter	z_1	z_2	z_3	h_1	h_2
Dimension (mm)	15.2	3.81	25.1	0.127	1.27

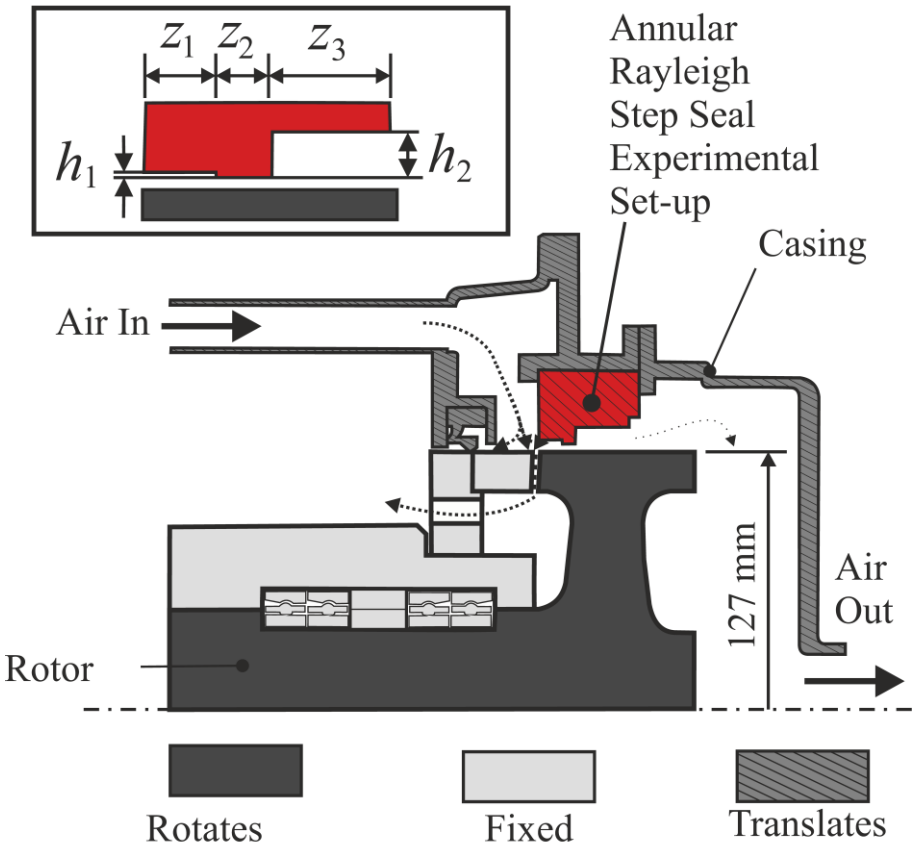

Figure 5: Cross-section of the test facility with a fixed Rayleigh step seal.

The electromagnetic shaker was used to excite the seal and its housing while the rotor was effectively held by a stiff bearing system. The relevant equation of motion for moving the seal and housing is

$$\mathbf{M}\,\ddot{\boldsymbol{\psi}} + \mathbf{C}\,\dot{\boldsymbol{\psi}} + \mathbf{K}\,\boldsymbol{\psi} = \mathbf{F_{fluid}} \tag{20}$$

where $\mathbf{M}$, $\mathbf{C}$, and $\mathbf{K}$ are mass, damping, and stiffness matrices, respectively. $\boldsymbol{\psi}$ is the vector of displacements and $\mathbf{F}_{\text{fluid}}$ is the force generated by the fluid film. Rouvas and Childs [32] outline a method which can be used to transform Eq. (20) into the frequency domain, which leads to the frequency response function (FRF):

$$\mathbf{G} = \mathbf{K} + j\omega\mathbf{C} \tag{21}$$

where $\mathbf{K} = Re(\mathbf{G})$ and $\omega\mathbf{C} = Im(\mathbf{G})$.

This method was employed by Pedraza-Valle [20] at pressure differences of 2.4, 2.9, and 3.3 bar for rotational speeds from 100 to 1,575 rad/s. The shaker was used to excite the system with a chirp signal that increased from 10 to 150 Hz. The amplitude of excitation was no greater than 25% of the clearance. These test parameters were used in the current numerical model.

The modeled direct stiffnesses in Fig. 6 show good agreement with the experimental data; both show that there is a small increase in the stiffness with increasing rotational speed but that increasing the pressure drop significantly increases the stiffness of the fluid film. This is expected since the Bearing Number, Λ, from Eq. (2) is the only term that is dependent on rotational speed. The change in Λ is very small compared with the change in the pressure-dependent terms. Additionally, Eqs. (10) and (15) show that the stiffness of the fluid film is directly dependent on the pressure difference through the seal.

Figure 7 compares the numerical direct damping coefficients with experimental values. In the studies conducted by Pedraza-Valle [20], the direct damping coefficient was found to be highly dependent on the temperature of the test facility, as shown in

Fig. 8. The 2.9 bar pressure drop tests were conducted at a lower temperature than the 2.4 and 3.3 bar experiments due to the test facility warming up through use.

It is evident from Figs. 7 and 8 that the direct damping follows an inversely proportional trend with temperature, and that the variance in temperature has a greater impact than the increase in pressure difference. Due to the small change in temperature, this has been attributed to variances in characteristics of the test rig rather than changes in the fluid properties [20].

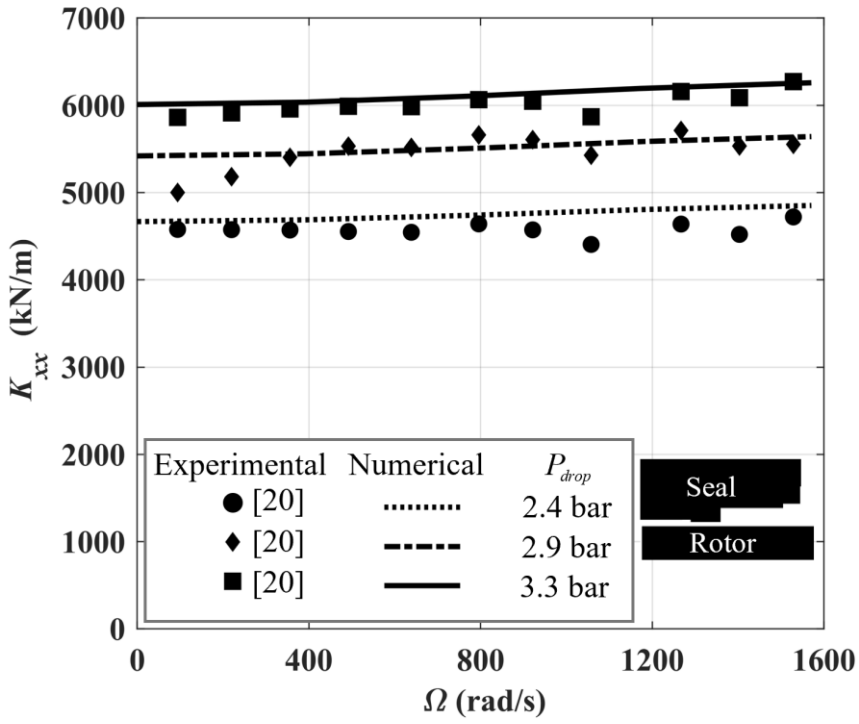

Figure 6: Direct stiffness for the fixed Rayleigh step seal compared with experimental data from Pedraza-Valle [20].

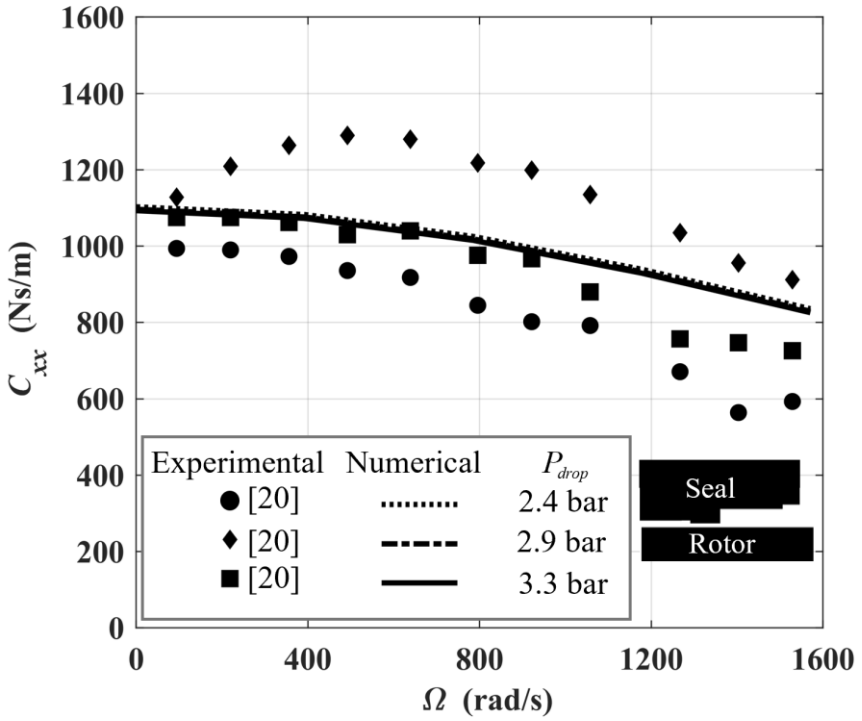

Figure 7: Direct damping for the fixed Rayleigh step seal for a range of excitation frequencies of 150 Hz, compared with experimental data from Pedraza-Valle [20].

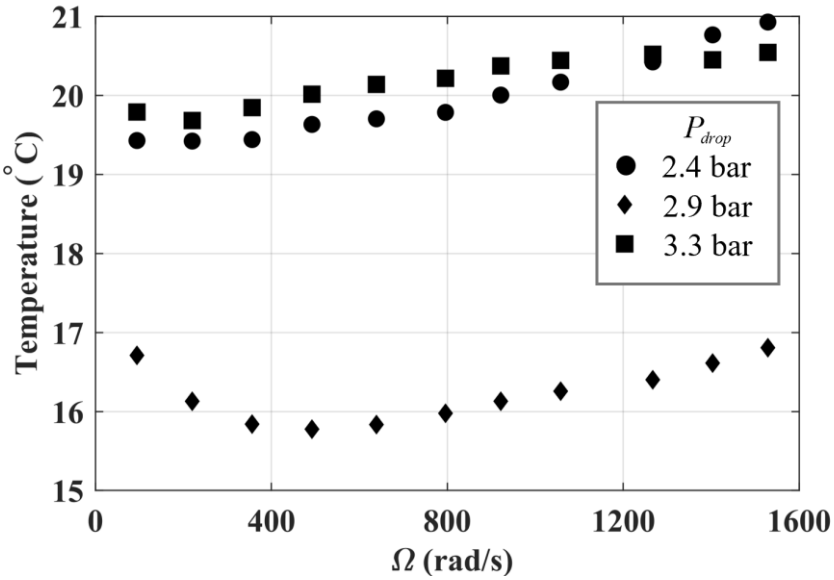

Figure 8: Temperature variation during measurements of the Direct damping for the fixed Rayleigh step seal [20].

Considering the 2.4 and 3.3 bar pressure drop results in Fig. 7, both the experimental and numerical results show a decrease in damping coefficient with an increase in rotational speed. This is caused by the reduction in clearance with the disk growth which effectively increases the Bearing and Squeeze Numbers, σ and Λ, in Eq. (2).

The leakage tests were conducted at a range of pressure drops up to 3.5 bar and three rotational speeds: 0, 730, and 1,250 rad/s. The experimental study found that the mass flow decreased with increased rotor speed, which correlated with the growth of the rotor.

Table 2 compares the measured growth of the shaft and the theoretical change in diameter using the one-dimensional model from Vullo and Vivio [33]. The effective clearance can be derived from the measured mass flow:

$$s_{eff} = \frac{\dot{m}_{exp}\sqrt{T_{ups}}}{2\pi p_{ups} r Q_\gamma} \tag{22}$$

where Q_γ is dependent on the pressure ratio and fluid properties. The measured and theoretical growth show very good agreement with one another, but both are larger than the change in effective clearance.

Table 2: Change in clearance with rotational speed, adapted from [20].

	Rotational Speed (rad/s)	
	730	1,250
Δ effective clearance (μm)	9.4	23.7
Δ measured growth (μm)	9	29
Δ model growth (μm)	9.55	28.06

The pressure profile calculated using the model can be used to evaluate the mass flow rate, $\dot{m}$, by integrating the axial velocity at any axial position over the clearance annulus:

$$\dot{m} = -\frac{1}{2\mu}\rho R \iint \frac{\partial p}{\partial z}\, \eta(h-\eta)\, d\eta\, d\theta \tag{23}$$

where ρ is the density and μ is the viscosity of the working fluid, $\partial p/\partial z$ is the pressure gradient along the axis of the rotor which was calculated using Eqs. (3) – (5) and $0 \leq \eta \leq h(\theta, Z)$ is the cross-film coordinate [34]. The density was calculated assuming ideal gas behavior as a function of the measured upstream conditions to model choked flow. The theoretical change in the rotor growth was included in the geometry of the mass flow model for non-zero rotational speeds, as shown in Fig. 9.

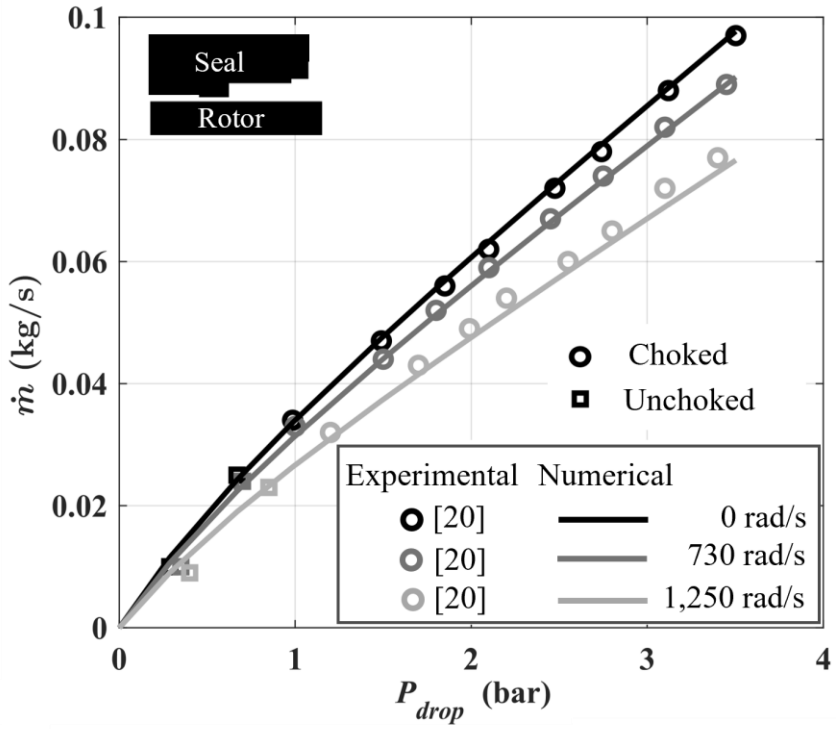

Figure 9: Leakage flow for the fixed Rayleigh step seal with rotor growth included in the numerical model which is compared with experimental data from Pedraza-Valle [20].

Figure 9 shows excellent agreement at the tested pressure drops compared with the numerical results for the leakage tests. The reduction in effective clearance caused by the rotor growth accounts for the reduction in mass flow in the model. Both the experimental and theoretical results show a steeper increase in mass flow at lower pressure drops until the flow is choked.

4 MODELING COMPLIANT SEAL BLOW DOWN

This section extends the numerical model to describe the behavior of an adaptive compliant seal, specifically the FRPALS with a Rayleigh step as shown in Fig. 2. The complete FRPALS is made from eight decoupled segments that can move toward the rotor to form a complete ring. The model in this section is validated against experimental measurements of a single segment incorporating supporting compliant leaves and fluid film forces during blow down.

4.1 Experimental Blow Down Characterization

Rahmani *et al.* [35] showed that the optimum position of a Rayleigh step is dependent on the pressure at the boundaries of the stepped component. Additionally, Pedraza-Valle [20] found that the position of the step affected the leakage flow through the FRPALS. In this paper, two different geometries of runner have been studied with the position of the step varied as shown in Figs. 10 (a) and 10 (b), referred to as P1 and P2, respectively.

The complete geometry for P1 was described by Pedraza-Valle *et al*. [31] and the step lengths are summarized in Table 1. The overall length of the runner and z_3 were increased by 6.35 mm to bring the step further forward for P2.

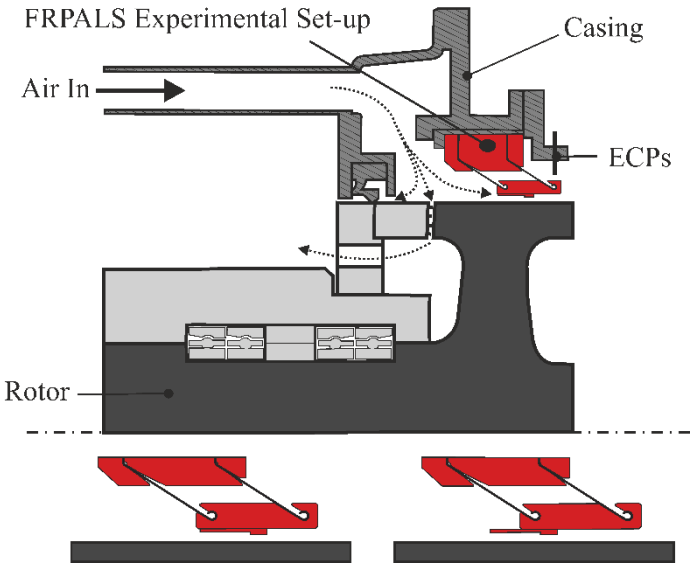

Figure 10: Cross-section of the test facility with different FRPALS configurations: (a) P1 and (b) P2.

As the FRPALS is adaptive, the movement of the runner under pressure loading was measured. Sensonics PRS02/7.0U01 Eddy-current probes (ECPs) were used to determine the displacement of the runner, as shown in Fig. 11.

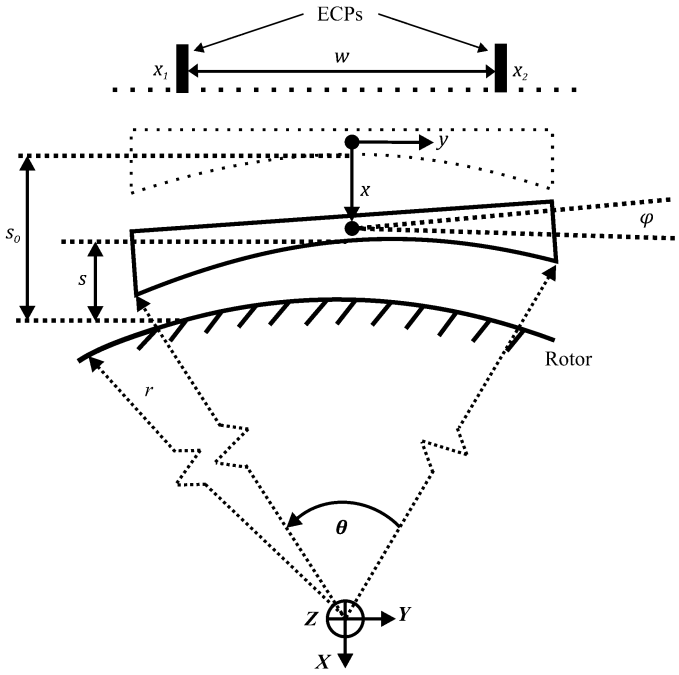

Figure 11: Positions of the ECPs targeting the top surface of the runner and geometric nomenclature convention.

The initial clearance, s_0, was determined using a feeler gauge at the mid-point of the runner. The same approach was used to find the initial clearance at the two radial extremes of the runner, to calculate the initial difference between the two sides prior to experimentation. In this study, the FRPALS is made of eight segments and $\theta = 45°$. Any difference in displacement between the two sides may be referred to as the 'rock angle', φ, an axial rotation of the runner:

$$\varphi = \tan^{-1}\left(\frac{x_1 - x_2}{w}\right) \tag{24}$$

where x_1 and x_2 are displacements of the two sides and w is the distance between the probes. There is a need for the leaves of FRPALS to accommodate the rock angle, as

the runners must be allowed to pivot to adapt to rotor eccentricities. The central displacement is

$$x = \frac{x_1 + x_2}{2} = s_0 - s \tag{25}$$

The following numerical model can be used to predict 2D displacement in terms of x and φ. Eq. (24) and (25) can then be used to compare the numerical results with the experimental displacements x_1 and x_2.

4.2 Numerical Model of the FRPALS

The stiffness and damping characteristics of the fluid film and leaves can be used to model the blow down behavior of the FRPALS, Fig. 12 shows the interactions between the mechanical and fluid components of the seal when subject to a pressure drop.

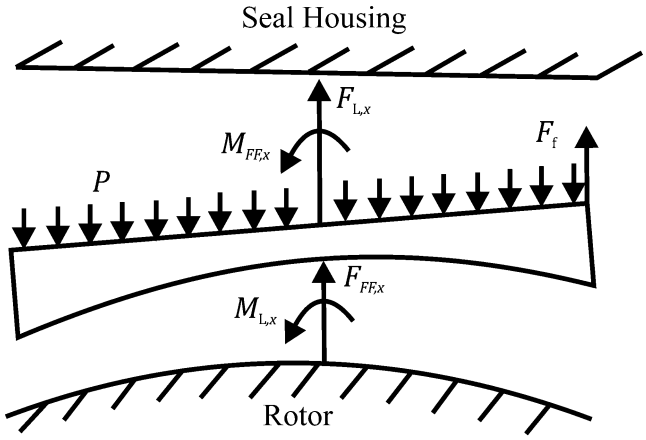

Figure 12: 2D Free-Body Diagram of the FRPALS subject to pressure with flow into the page with degrees of freedom shown in Fig. 10.

The total force and moment acting on the runner can be used to set the equations of motion:

$$\sum F = m\ddot{x} \qquad \sum M = I\ddot{\varphi} \tag{26}$$

where the force from the fluid film is dependent on the stiffness and damping characteristics of the gas. The direct dynamic coefficients, K_{xx} , K_{yy} , C_{xx}, and C_{yy}, may be evaluated for a given runner film profile at each position, s, and pressure, P, according to methodology described in Section 3. The rotational stiffness and damping coefficients may be derived from the translational coefficients for a single runner by noting from Fig. 10 that a relative side shift, y, of the runner induces an equivalent $\varphi = y/r$ since the rotor radius will be much larger than any film thickness. It follows that the rotational coefficients are given by

$$K_{\varphi}(s,P) = K_{yy}(s,P)r^2 \qquad C_{\varphi}(s,P) = C_{yy}(s,P)r^2 \tag{27}$$

Maps of these coefficients against all possible positions, s, and pressures, P, may be generated and stored in look-up tables for use in dynamic simulations. Examples of these maps for P1 without shaft rotation are shown in Figs. 13 and 14.

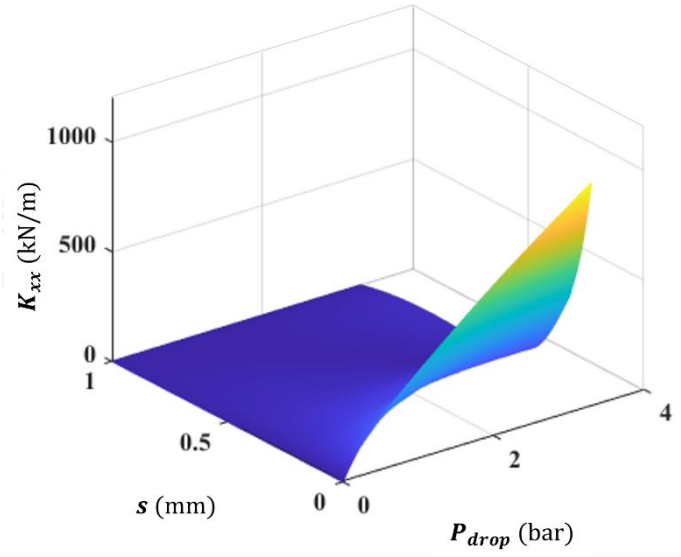

(a)

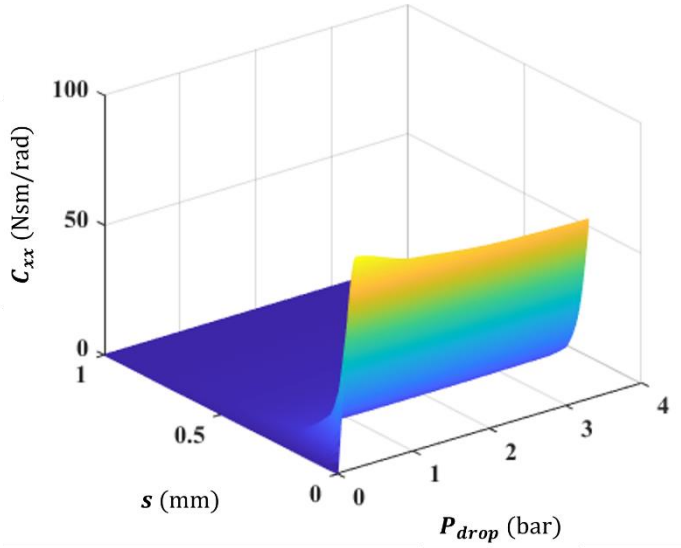

(b)

Figure 13: Translational fluid film (a) stiffness and (b) damping coefficients variance with pressure drop and distance from design clearance at a frequency of 150 Hz.

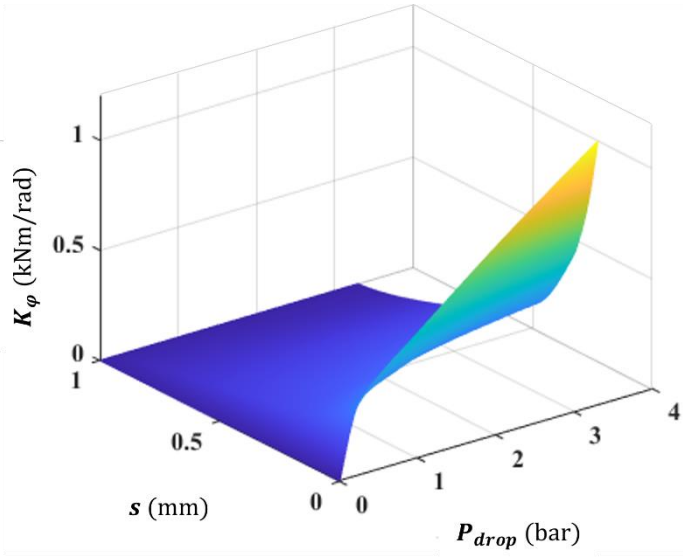

(a)

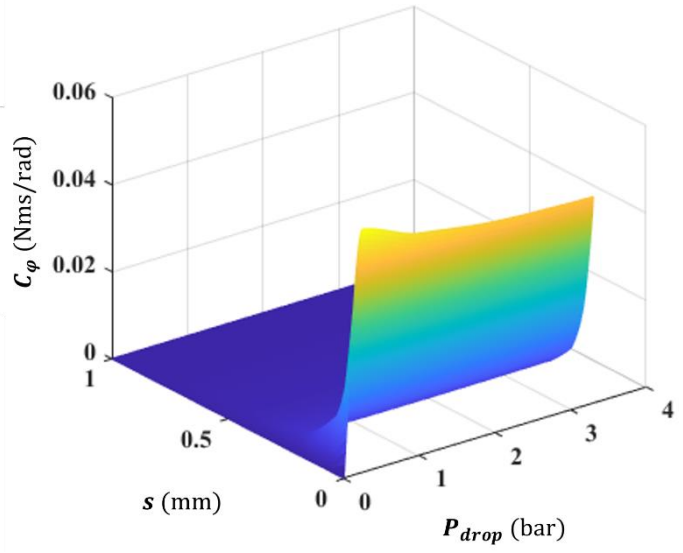

(b)

Figure 14: Rotational fluid film (a) stiffness and (b) damping coefficients variance with pressure drop and distance from design clearance at a frequency of 150 Hz.

The dynamic coefficient maps in Figs. 13 and 14 show a significant increase in stiffness and damping as the clearance reduces. The stiffness coefficients are also shown to increase with the pressure difference. The Reynolds equation is classically

used for thin fluid films in bearing and lubrication applications. To ensure the accuracy of the coefficient maps the criterion outlined by Bailey [36] was used, who developed a modified form of the Reynolds Number:

$$Re^* = \frac{\rho u L}{\mu}\left(\frac{s}{L}\right)^2 \tag{28}$$

If the modified number is less than unity, $Re^* < 1$, then the Reynolds equation will be dominated by the pressure and viscosity terms, ensuring the thin fluid film assumptions are accurate [36]. Figure 15 shows the operational envelopes for the tests conducted in this study. Larger initial clearances means that Re^* falls outside of this range, as shown in Fig. 15. This causes the model to oscillate until the seal has blown down to within a clearance for the Reynolds equation to be highly accurate.

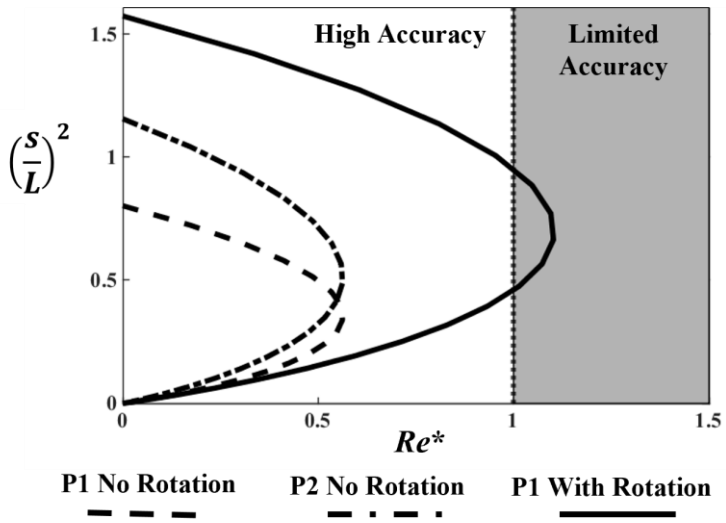

Figure 15: Operational envelopes of the blow down tests compared with modified Reynolds number showing that Reynolds equation has limited accuracy for the initial conditions during the P1 rotation tests.

The characteristics of the leaves were measured experimentally using an Instron Tensile Tester. A known rate of displacement was applied to the specimen the load required to extend the specimen was measured. A surrogate runner that could hold two pairs of leaves mounted symmetrically about a central plane was used so that it could be loaded in the vertical axis of the tensile test machine, as shown in Fig. 16. The leaves were displaced up to a maximum deflection of 4 mm to ensure that no permanent plastic deformation occurred. Figure 16 shows the combined force against displacement profile for the two sets of leaves. The stiffness, K_L, of a single leaf pair can be found from the combined stiffness and evaluated as $K_L = 47$ kN/m.

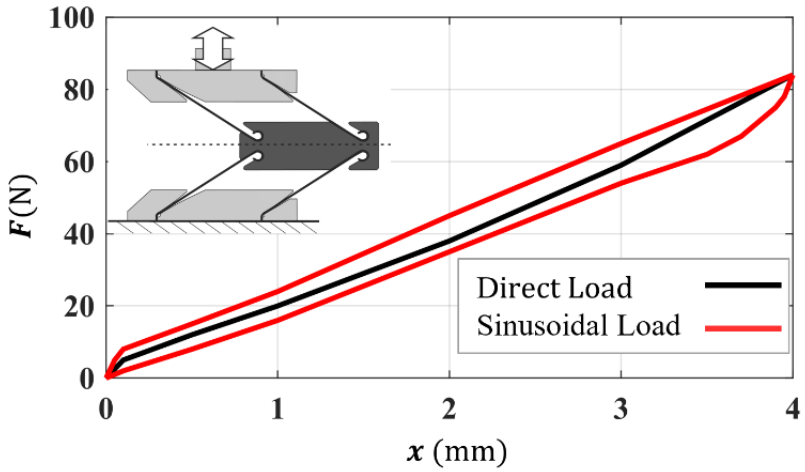

Figure 16: Tensile test, including double-sided runner.

The tensile tester was also used to apply a sinusoidal load, $F(t)$, shown in Fig. 16. The hysteresis loop exhibited was used to evaluate the work done per cycle, W, which may be attributed to dry (Coulomb) friction in the knuckles of the leaves within the runner. This was then used in turn to calculate the equivalent Coulomb friction force observed in the hysteresis loop:

$$F_L = \mu N = \frac{1}{2}\frac{W}{4X} \tag{29}$$

where X is the displacement amplitude. This approach was used to evaluate a friction force of approximately 2 N when loading, and 4 N when unloading the leaves. The experimental values of L and μN were used in the model shown in Fig. 12 incorporated in the terms $F_{L,x}$ and $M_{L,\varphi}$. When subject to the pressure force, and assuming that any other external force is negligible, the 2D model can be described in matrix notation

$$\begin{bmatrix} m & 0 \\ 0 & I \end{bmatrix}\begin{bmatrix} \ddot{x} \\ \ddot{\varphi} \end{bmatrix} + \begin{bmatrix} C_x & 0 \\ 0 & C_\varphi \end{bmatrix}\begin{bmatrix} \dot{x} \\ \dot{\varphi} \end{bmatrix} + \begin{bmatrix} K_x & 0 \\ 0 & K_\varphi \end{bmatrix}\begin{bmatrix} x \\ \varphi \end{bmatrix} = \mathbf{F_0} \tag{30}$$

where

$$\begin{gathered} K_x = K_{xx}(s,P) + K_L \\ C_x = C_{xx}(\mathrm{s},P) \\ \mathbf{F_0} = \frac{1}{2}\begin{bmatrix} 2(F_P(t) - F_f(t) - F_L) \\ F_f\,(t)L \end{bmatrix} \end{gathered} \tag{31}$$

where K_{xx}, C_{xx}, K_φ and C_φ are determined from the dynamic coefficient maps shown in Figs. 13 and 14 and m and I are the mass and second moment of area of the runner respectively. Eq. (30) shows that the dynamic system will accelerate when subject to an increasing pressure load but will reach a steady-state equilibrium as the stiffness terms increase with pressure. Eq. (31) and Figs. 13 and 14 show that the dynamic coefficients of the fluid film are dependent on the clearance and pressure drop across the seal. C_x will be negligible for large clearances but increase as the seal blows down.

This 2D model also incorporates a friction force, F_f, to replicate any interaction between the runner and a neighboring segment, as shown in Fig. 12. The friction force can be assumed to be a fraction, τ, of the total force on the runner that opposes the direction of motion:

$F_f(t) = \tau F_{Total}(t)$	(32)

For the purposes of the model presented in this study, it has been assumed that that τ is within the expected range of friction coefficient for the material of the runner, where τ = 0.36.

The displacement and rock angle of the runner may be found from Eqs. (26) and (30) through the double integration of the time dependent translational and angular accelerations respectively. Figure 17 shows the experimental and numerical displacement and rock angle for runner P2 during pressurization.

The initial clearance was found to be approximately 1.1 mm and the pressure difference was increased over 20 s. In the absence of rotation, the runner remained in a steady position once blown down.

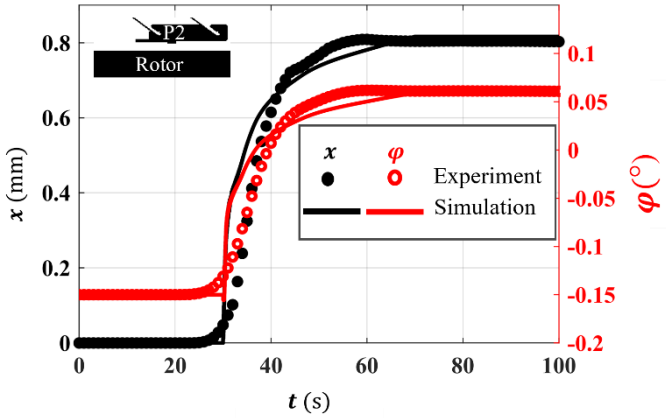

Figure 17: Displacement and rock angle of the FRPALS with runner P2 without shaft rotation.

It is apparent that the dynamic model shown in Fig. 17 can accurately predict the blown down and rocked positions from the rest. However, the model displaced at a greater rate than was observed experimentally. This was attributed to a constant friction factor, whereas in practice it will vary as the runner pressurized and interacted more with the neighboring component through actuation.

Figure 18 shows the displacement and rock for P1 for an increasing pressure difference, with and without rotation. The initial offset was 1.1 mm without shaft rotation and 1.8 mm at 200 rad/s, leading to a larger displacement.

Figure 18 (a) shows that the model accurately captured the translational and angular displacements with the runner in P1. There was a slight drift in the experimental results across the 600 s that the runner was in the blown down position, which led to a small discrepancy between the initial and final position of the runner, highlighting the difference between the model and experimental results during depressurization. Figure 18 (b) shows that the FRPALS oscillated from the blown down position in the experimental facility which was not shown in the simulation. This is due to fluctuations

in the hydrodynamic forces in the test rig with rotation which are not represented in the model. However, the model accurately captures the magnitude of displacement and both the model and experimental results show that the runner returned to approximately the initial position when depressurized.

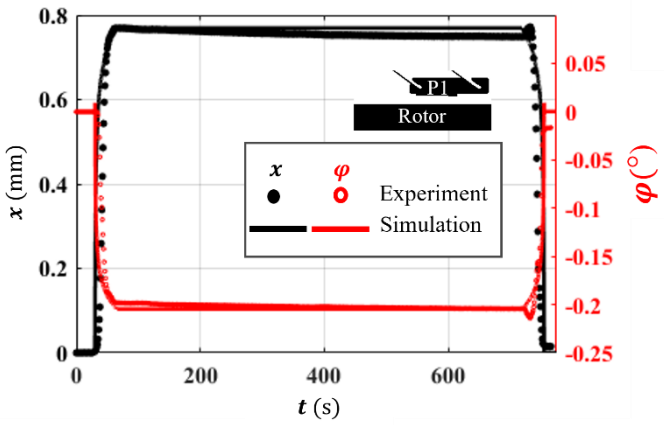

(a)

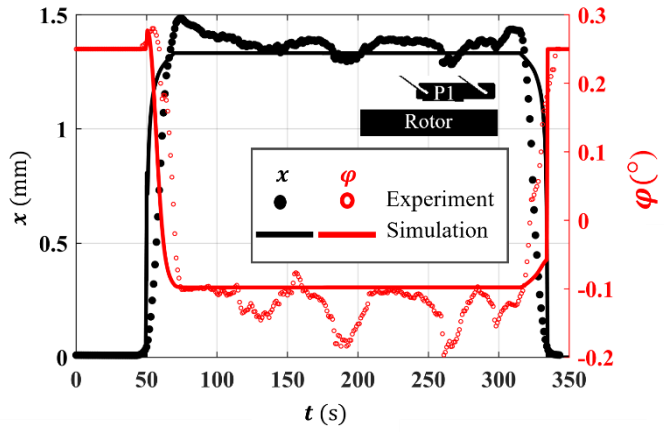

(b)

Figure 18: Displacement and rock angle of the FRPALS with runner P1 at (a) 0 rad/s and (b) 200 rad/s shaft speed.

Figure 19 presents the experimental and numerical results of the change in clearance and rock angle for runner P1. The clearance of the seal has been normalized with the area subjected to the flow:

$$\overline{s} = \frac{s}{r_{eq}} \quad (33)$$

where r_{eq} is the equivalent radius of the seal housing, which was found through the cross-sectional area of the segments of the FRPALS subjected to the flow. The initial dimensionless clearance in the experimental facility with P1 installed was found to be 0.065 and 0.06 for x_1 and x_2, respectively.

The 2D numerical model is shown to accurately predict the blow down and rock angle of the FRPALS. There is a small variation between the experimental measurements under pressurizing and depressurizing conditions, indicating a hysteretic effect. This can be attributed to the frictional forces found during the tensile tests. However, the experimental results show a larger hysteresis than the numerical model.

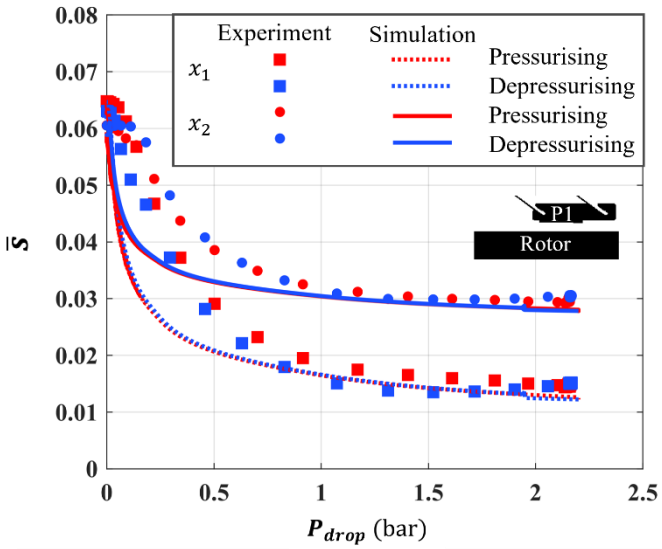

(a)

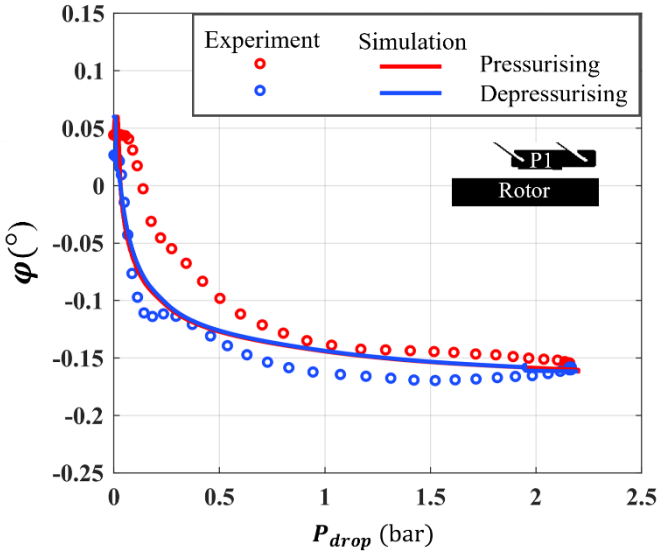

(b)

Figure 19: Radial behavior of the FRPALS with runner P1 in terms of change in (a) clearance and (b) rock angle with increasing pressure difference, without shaft rotation.

This may be attributed to the difficulty in accurately determining the friction force, and the fact a simple Coulomb model was used to fit the tensile tests. In the experimental study, it is likely that this frictional interaction between components changed as the runners closed toward the rotor. This is because the gap between the FRPALS segments reduced and so the forces between them will tend to increase.

Figure 20 compares the experimental and numerical radial behavior of the FRPALS with the runner in P2. The initial clearance was found to be different from the experimental set-up in Fig. 19 owing to the fact that the seal was rebuilt to accommodate the alternative runner.

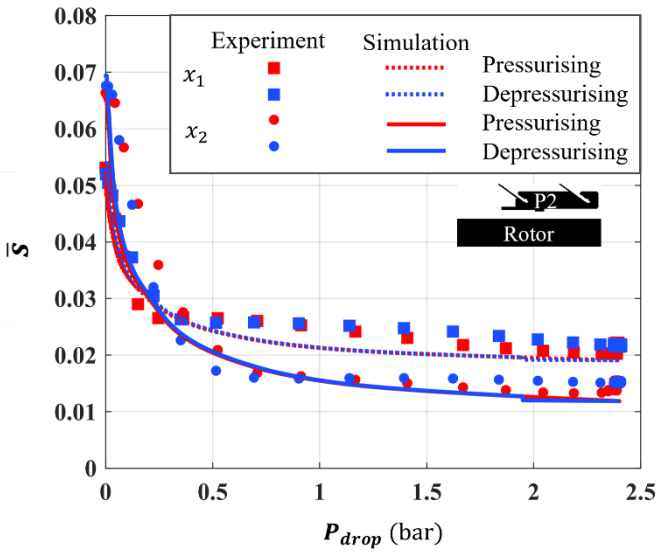

(a)

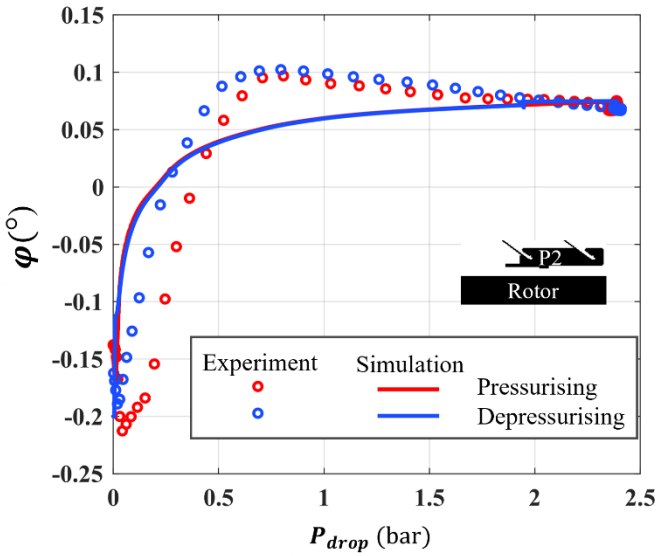

(b)

Figure 20: Radial behavior of the FRPALS with runner P2 in terms of change in (a) clearance and (b) rock angle with increasing pressure difference, without shaft rotation.

Figure 20 again shows good agreement between the numerical model and experimental results for both the change in clearance and rock angle of the FRPALS. The initial rock angle changed from the study with the runner in position P1. This can be attributed to the difference between the initial clearances, s_0, of the two sides of the runner, x_1 and x_2 after rebuilding the seal with the geometry P2. Subsequently, the rock angle shown in Fig. 20 (b) increases with pressure rather than decreasing as exhibited in Fig 16 (b).

When comparing Figs. 19 (a) and 20 (a), increasing the length of the runner causes the FRPALS to blow down to a smaller clearance at operational conditions. Additionally, the longer runner, P2, causes the seal to close under lower pressure differences than those of P1. This is expected, as the upstream pressure directly correlates to the force that closes the seal; therefore, the surface area must be closely controlled to ensure that the seal blows down to the desired design clearance. The runner in position P2 had a smaller operational clearance than the runner in P1. This would correspond to a decreased leakage flow through the seal as was observed by Pedraza-Valle [20].

Figure 21 compares the radial behavior of the FRPALS with the runner in P1 with the shaft rotating at 200 rad/s. During the experimental set-up, the initial clearance was once again found to be different from the static tests, and larger than that exhibited in Figs. 19 and 20.

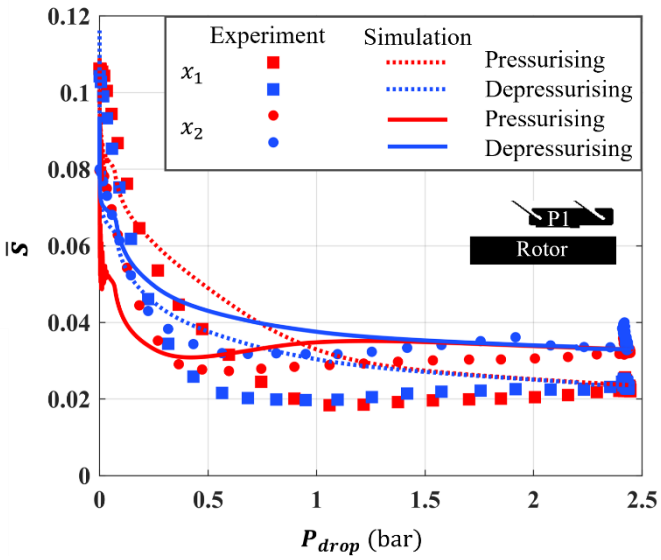

(a)

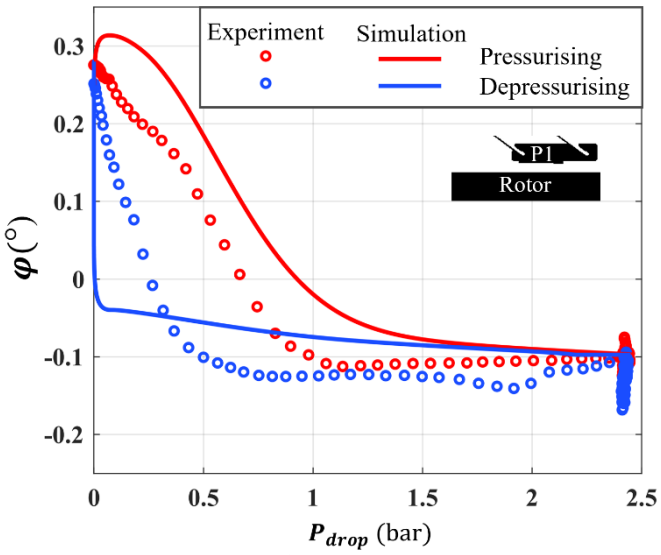

(b)

Figure 21: Radial behavior of the FRPALS at 200 rad/s with runner P1 in terms of change in (a) clearance and (b) rock angle, with increasing pressure difference.

The results in Fig. 21 show a similar trend to the static tests in Figs. 19 and 20. During pressurization the numerical model exhibits larger oscillatory motion than was observed in the experimental values. This can be attributed to the inertial forces dominating the fluid film, rather than the pressure and viscosity forces [36].

The runner deflects under pressure toward the rotor and film rides at a dimensionless clearance of approximately 0.03, which is comparable with the static P1 test. At the blown down condition, the runner position fluctuated during the test. This is due to the varying hydrodynamic forces under the step as the shaft rotates, which is not captured in the model or present in the static experiments.

5 CONCLUSIONS

A numerical model has been developed which applies the Reynolds equation to accurately predict the dynamic coefficients and leakage behavior of a static Rayleigh step seal for varying pressure differences and rotational speeds. The model was validated against experimental measurements of stiffness and damping coefficients. It showed a small increase in the direct stiffness and a decrease in direct damping with increased rotational speed. This was attributed to the decrease in clearance caused by the growth of the rotor. This also influenced the predicted and measured leakage performance of the static seal, which decreased with rotor growth as expected.

The incorporation of the dynamic coefficients into a 2D blow down model enabled the prediction of the translational and rock angle displacement paths of the FRPALS. These were compared with new experimental displacement measurements from the dynamic test facility using eddy current probes targeting a single-segment seal. The

rock angle was shown to be highly dependent on the initial installation clearances across the width of the runner and changed as the FRPALS was blown down. The translational displacements of the runner were accurately predicted as a function of the dynamic coefficients. By testing two different seal geometries without shaft rotation, it was shown that the magnitude of displacement and film-riding clearance is dependent on the position of the Rayleigh step and length of the runner. The model also gave good agreement with the clearance and rock angle measurements tested with shaft rotation for one of the runner positions.

The method developed in this study could be used in the future to predict the movement of a complete eight-segment FRPALS, and modifications could enable its application to alternative seal designs featuring a Rayleigh step. Additional development would also allow for the prediction of dynamic coefficients for adaptive seals.

ACKOWEDLEGEMENTS

The technical support of Andrew Langley, Jim Cansell, and Daniel Ball enabled the continued use of the test facilities, the authors are extremely grateful. Manojhan Sivarajah is also thanked for his assistance in initial development of the model.

NOMENCLATURE

C	Damping Coefficient (Ns/m)
K	Stiffness Coefficient (N/m)
F	Force (N)
H	Dimensionless Film Thickness (h/s)

HP	High Pressure
h	Film Thickness (m)
I	Moment of Inertia of Runner (m^4)
L	Axial Length of Film (m)
LP	Low Pressure
m	Mass of Runner (kg)
P	Dimensionless Pressure (p/p_{atm})
p	Pressure (Pa)
Q	Dependent Variable (P^2H^2)
r	Rotor Radius (m)
T	Temperature (°C or K)
t	Time (s)
u	Fluid Velocity (m/s)
W	Work Done (J)
w	Width Coordinate (m)
X	Dimensionless Perturbation Coordinate (x/c)
x	Displacement in X (m)
Y	Dimensionless Perturbation Coordinate (y/c)
y	Displacement in Y (m)
Z	Dimensionless Axial Coordinate (z/c)
z	Axial Coordinate in Z (m)
Λ	Bearing Number
σ	Squeeze Number

μ	Kinematic Viscosity (m^2/s)
μN	Force due to Coulomb Damping (N)
ρ	Density (kg/m^3)
φ	Rock Angle (°)
τ	Friction Function
Ω	Rotational Speed (rad/s)
ω	Excitation Frequency (rad/s)
Θ	Circumferential Coordinate (rad)

SUBSCRIPTS

aa, ab	General Rotordynamic Coefficient
eff	Effective Parameter
ex, ey	Complex Solution
exp	Experimental Value
f	Friction
L	Leaf Characteristic
ups	Upstream Value
xx, xy	Direct Rotordynamic Coefficient
xy, yx	Cross-Coupled Rotordynamic Coefficient
0	Initial Solution or Condition

REFERENCES

[1] H. F. Black, "Effects of Hydraulic Forces in Annular Pressure Seals on the Vibrations of Centrifugal Pump Rotors," *Journal of Mechanical Engineering Science,* vol. 11, no. 2, pp. 206-213, 1969.

[2] D. Childs, "Simulation Models for Flexible Spinning Bodies," *Simulation,* vol. 12, no. 6, pp. 291-296, 1969.

[3] S. P. Arthur and D. W. Childs, "Measured Rotodynamic and Leakage Characteristics of a Tooth-on Rotor Labyrinth Seal with Comparisons to a Tooth-on-Stator Labyrinth Seal and Predictions," in *Proceedings of the ASME Turbo Expo 2015: Turbine Technical Conference and Exposition*, Montreal, 2015.

[4] O. Matsushita, M. Tanaka, M. Kobayashi, P. Keogh and H. Kanki, Vibrations of Rotating Machinery: Volume 2. Advanced Rotordynamics: Applications of Analysis, Troubleshooting and Diagnosis, Springer, 2019.

[5] O. Reynolds, "IV. On the theory of lubrication and its application to Mr. Beauchamp tower's experiments, including an experimental determination of the viscosity of olive oil," *Philosophical Transactions of the Royal Society of London,* vol. 177, 1886.

[6] D. L. Rhode and M. J. Guidry, "A new approach for stabilizing labyrinth seal leakage," *Tribology Transactions,* vol. 36, no. 2, pp. 219-224, 1993.

[7] R. E. Burcham, "Liquid Rocket Enginge Turbo Pump Rotating-Shaft Seals, Ohio," *National Aeronautics and Space Administration,* 1978.

[8] R. E. Chupp, R. C. Hendricks, S. B. Lattime, B. M. Steinetz and M. F. Aksit, "Turbomachinery Clearance Control," in *Turbine Aerodynamics, Heat Transfer, Materials and Mechanics*, American Institute of Aeronautics and Astronautics, Inc, 2014, pp. 61-188.

[9] J. G. Feruson, "Brushes as High Performance Gas Turbine Seals," in *ASME 1988 International Gas Turbine and Aeroengine Congress and Exposition*, Amsterdam, 1988.

[10] Y. Ha, T. Ha, J. Byun and Y. Lee, "Leakage Effects due to Bristle Deflection and Wear in Hybrid Brush Seal of High-Pressure Steam Turbine," *Tribology International,* vol. 150, no. 1, 2020.

[11] L. San Andrés and A. Anderson, "AN ALL-METAL COMPLIANT SEAL VERSUS A LABYRINTH SEAL: A COMPARISON OF GAS LEAKAGE AT HIGH TEMPERATURES," in *Proceedings of ASME Turbo Expo 2014: Turbine Technical Conference and Exposition*, Düsseldorf, Germany, 2014.

[12] J. Justak, "Hydrogen Compressor Seal Case Study - Utilizing HALO (Non-Contacting, Compliant) Inter-Stage, Impeller Eye, Buffer and Fail-Safe Seals," 2013.

[13] H. Nakane, A. Maekawa, E. Akita, K. Akagi, T. Shinorhara and H. Uehara, "The Development of High Performance Leaf Seals," in *ASME Turbo Expo 2002: Power for Land, Sea, and Air*, Amsterdam, 2002.

[14] I. H. Jahn, D. Gillespie and P. Cooper, "Hydrodynamic air-riding in leaf seals," in *Proceedings of ASME Turbo Expo 2013: Turbine Technical Conference and Exposition*, San Antonio, Texas, 2013.

[15] C. Grondahl, "Pressure Actuated Leaf Seals for Improved Turbine Shaft Sealing," in *41st AIAA/ASME/SAE/ASEE Joint Propulsion Conference and Exhibit*, Tuscon, 2005.

[16] C. M. Grondahl, "Pressure Actuated Leaf Seal Feasibility Study and Demonstration," in *45th AIAA/ASME/SAE/ASEE Joint Propulsion Conference & Exhibit*, Denver, Colorado, 2009.

[17] A. Bowsher, P. Crudgington, C. Grondahl, J. Dudley, T. Kirk and A. Pawlak, "Pressure Activated Leaf Seal Technology Readiness Testing," *Journal of Engineering for Gas Turbines and Power,* vol. 137, no. 6, 2015.

[18] J. Pasch and D. Stapp, "Testing of a New Turbocompressor for SUpercritical Carbon Dioxide Closed Brayton Cycles," in *ASME Turbo Expo 2018: Turbomachinery Technical Conference and Exposition,* Oslo, Norway, 2018.

[19] T. Kirk, A. Bowsher, P. Crudgington, A. Pawlak, C. Grondahl and J. Dudley, “Turbomachinery Technical Conference and Exposition,” in *AIAA/SAE/ASEE Joint Propulsion Conference: Propulsion and Energy Forum*, Salt Lake City, UT, 2016.

[20] E. Pedraza-Valle, Development of a rotating test facility for the experimental characterisation of shaft seals (Doctoral Thesis, University of Bath), 2020.

[21] L. Beermann, J. Wilhelm and H.-J. Bauer, “Measurements and Modeling of the Movement Behavior of a Radial Adaptive Seal,” *Journal of Engineering for Gas Turbines Power,* vol. 141, no. 11, 2019.

[22] C. M. Grondahl and J. C. Dudley, “Film Riding Leaf Seals for Improved Shaft Sealing,” in *ASME Turbo Expo 2010: Power for Land, Sea and Air*, Glasgow, 2010.

[23] K. Du, Y. Li, S. Suo and Y. Wang, “Dynamic Leakage Analysis of Noncontacting Finger Seals Based on Dynamic Model,” *Journal of Engineering for Gas Turbines and Power,* vol. 137, no. 9, 2015.

[24] M. T. C. Faria and L. San Andrés, “On the Numerical Modeling of High-Speed Hydrodynamic Gas Bearings,” *Journal of Tribology,* vol. 122, no. 1, pp. 124-130, 2000.

[25] R. P. Gabriel, “Fundamentals of Spiral Groove Non-Contacting Face Seals,” *Lubrication Engineering,* vol. 50, no. 3, pp. 215-224, 1994.

[26] M. T. C. Faria, “An Efficient Finite Element Procedure for Analysis of High-Speed Spiral Groove Gas Face Seals,” *Journal of Tribology,* vol. 123, no. 1, pp. 205-2010, 2001.

[27] X. Zhu and L. San Andrés, “Rotordynamic Performance of Flexure Pivot Hydrostatic Gas Bearings for Oil-Free Turbomachinery,” *Journal of Engineering for Gas Turbines and Power,* vol. 129, no. 4, pp. 1020-1027, 2007.

[28] A. Morley, Strength of Materials, Longmans, Green and Co. Ltd. ISBN 144462749X, 1954.

[29] V. Castelli and J. Pirvics, “Equilibrium Characteristics of Axial-Groove Gas-Lubricated Bearings,” *Journal of Lubrication Technology,* vol. 89, no. 2, 1967.

[30] J. W. Lund and K. K. Thomsen, “A Calculation Method and Data for the Dynamic Coefficients of Oil-Lubricated Journal Bearings,” *Dryrobes,* 1978.

[31] E. Pedraza-Valle , G. Papageorgiou, A. Bowsher, P. Crudgington, C. M. Sangan, P. S. Keogh and J. A. Scobie, “ON THE DEVELOPMENT OF A PRESSURE ACTUATED LEAF SEAL FOR TURBOMACHINERY APPLICATIONS,” in *ASME Turbo Expo*, Phoenix, Arizona, 2019.

[32] C. Rouvas and D. W. Childs, “A Parameter Identification Method for the Rotordynamic Coefficientsof a High Reynolds Number Hydrostatic Bearing,” *Journal of Vibration and Acoustics,* vol. 115, no. 3, pp. 264-270, 1993.

[33] V. Vullo and F. Vivio, Rotors: Stress analysis and design, Springer Science & Business Media, 2013.

[34] B. J. Hamrock, S. R. Schmid and B. O. Jacobson, Fundamental of Fluid Film Lubrication, Second Edition, New York. Basel.: Marcel Dekker, INC., 2004.

[35] R. Rahmani, A. Shirvani and H. Shirvani, “Analytical analysis and optimisation of the Rayleigh Step Slider Bearings,” *Tribology International,* vol. 42, no. 5, pp. 666-674, 2009.

[36] D. Bailey, “Limits of the Reynolds Equation for Negative Pressure Sliders,” *IEEE Transactions on magnetics,* vol. 31, no. 6, pp. 2979-2981, 1995.